

Supplement of

Response to Referee 1

Longlei Li et al.

ll859@cornell.edu

Received and published: 16 October 2020

The copyright of individual parts of the supplement might differ from the CC BY 4.0 License.

Table R1. Component oxides that an alkali feldspar such as $(\text{Na}_{0.87}\text{K}_{0.13})\text{Al}_1\text{Si}_3\text{O}_8$ consists of.

Oxide	Wt%	MolWt oxide	Moles oxide	Moles cation	Moles oxygen	Moles cations for 8O
SiO₂	68.2	60.086	1.135	1.135	2.2701	2.9997
Al₂O₃	19.29	101.963	0.1892	0.3784	0.5676	1.0001
Na₂O	10.2	61.9796	0.1646	0.3291	0.1646	0.8699
K₂O	2.32	94.2037	0.0246	0.0493	0.0246	0.1311

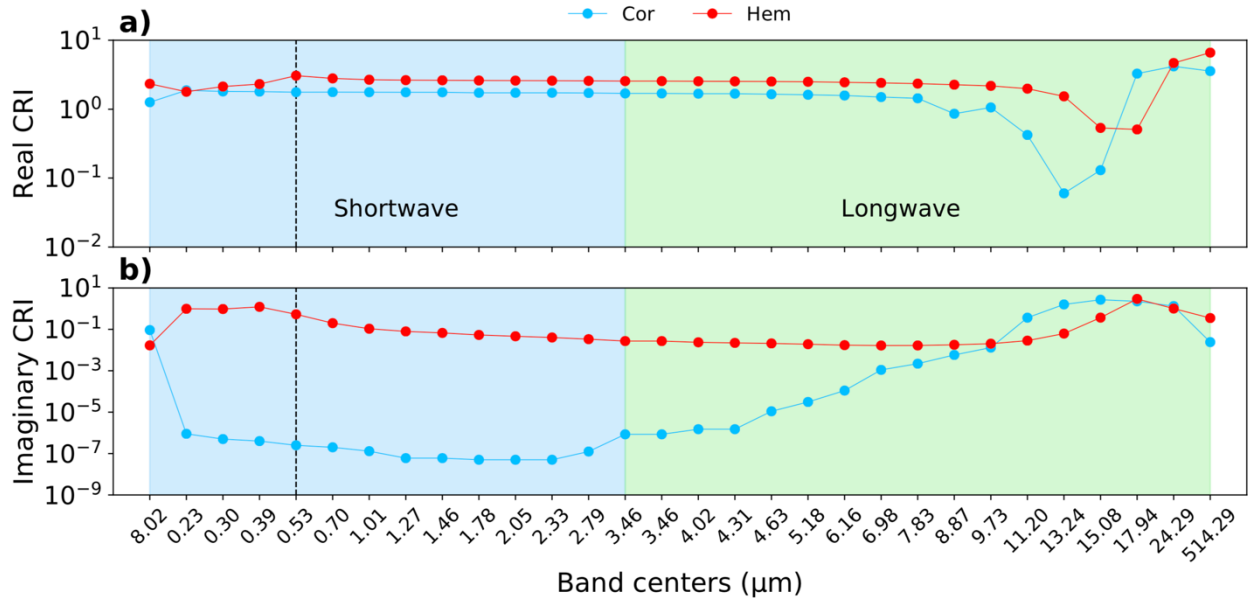


Figure R1. Real (a) and imaginary (b) complex refractive index (CRI) of Corundum (Cor) and hematite (Hem) for shortwave (blue shading) and longwave (green shading) bands (band centers shown as x-axis labels) implemented into CAM5/6. CRI values were derived for each band with original data from Scanza et al. (2015). Vertical dash lines indicate the shortwave Band 10 centered at 0.53 μm at which dust aerosol optical depth (DOD) and single scattering albedo were calculated (see Table 5 of the preprint) in CAM5/6. Note the band centered at 8.02 μm (leftmost) is broad with the boundaries of 3.84 and 12.20 μm . This broad band has been included in the model as shortwave bands by model developers.

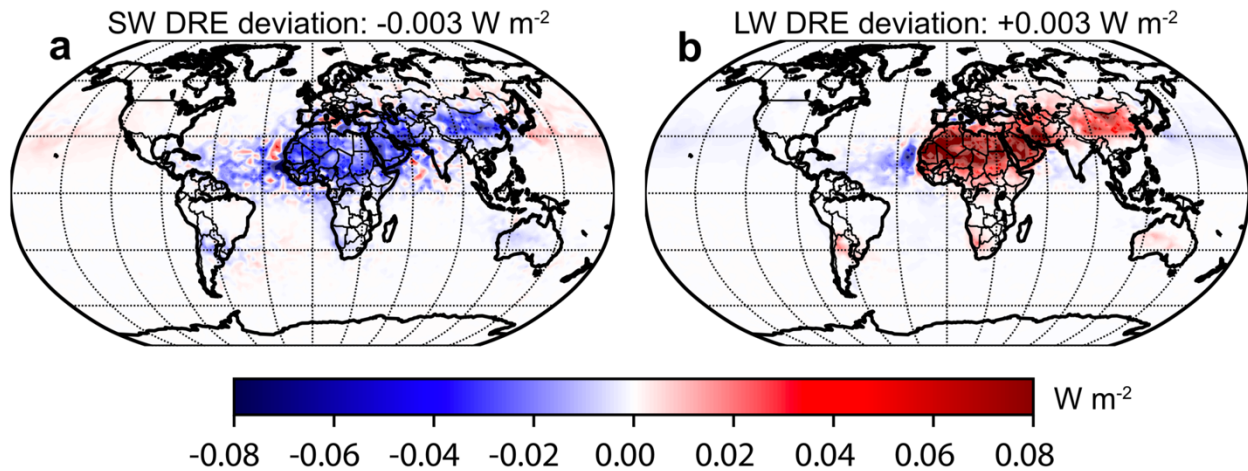


Figure R2: Upper branch of uncertainty in shortwave (SW; a,) and longwave (LW; b; with no 51% augment) dust direct radiative effect $W m^{-2}$ at the top of the atmosphere induced by uncertainty in aluminum oxide with the assumption that the spatial distribution and uncertainty are the same as quartz in the silt-sized category. Simulations were constructed using C1999. We replaced the optical properties of quartz by those of aluminum oxide (Fig. R1) with the complex refractive index taken from Table 2 of Toon and Pollack (1987). Numbers in the title denote global mean deviation from the “baseline” (new experiment in which we also replaced quartz in the silt-sized category with aluminum oxide) in CAM5.

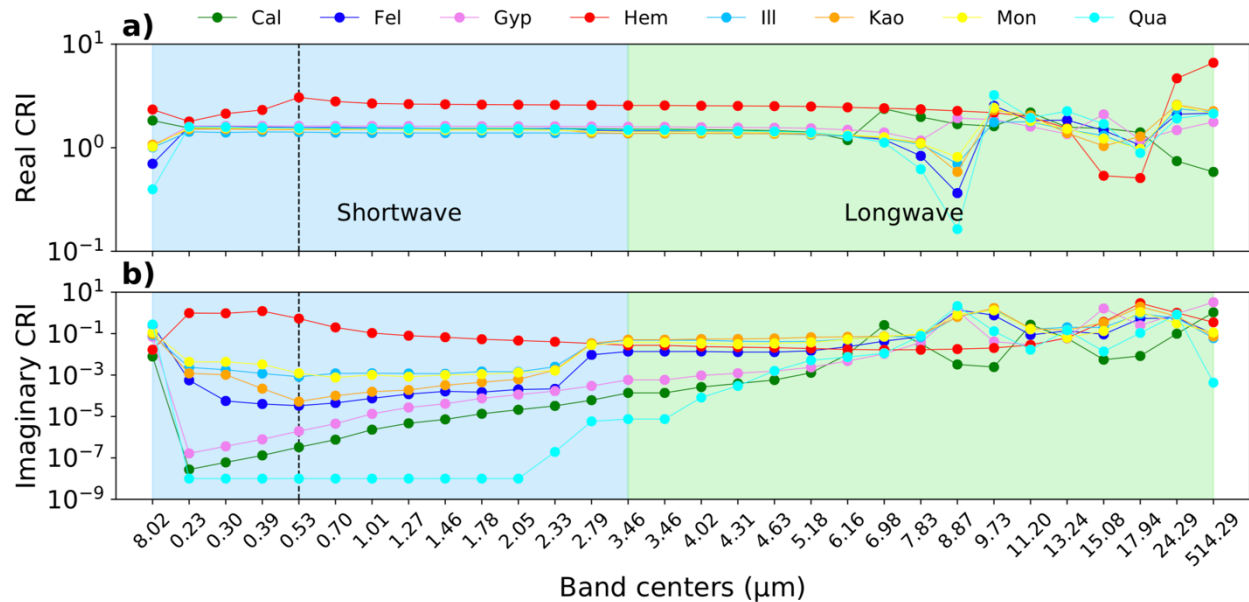


Figure R3. Real (a) and imaginary (b) complex refractive index (CRI) of each mineral for shortwave (blue shading) and longwave (green shading) bands (band centers shown as x-axis labels) implemented into CAM5/6. CRI values were derived for each band with original data taken from Scanza et al. (2015). The imaginary CRI of goethite was assumed to be half of hematite with the same spectral shape, while the real part of goethite is assumed to be identical as that of hematite. Vertical dash lines indicate the shortwave Band 10 centered at 0.53 μm at which dust aerosol optical depth and single scattering albedo for CAM5/6 were calculated (see Table 5 of the preprint). Note the band centered at 8.02 μm (leftmost) is broad with the low and high boundaries of 3.84 and 12.20 μm , respectively. This broad band has been included in the model as shortwave bands by model developers.

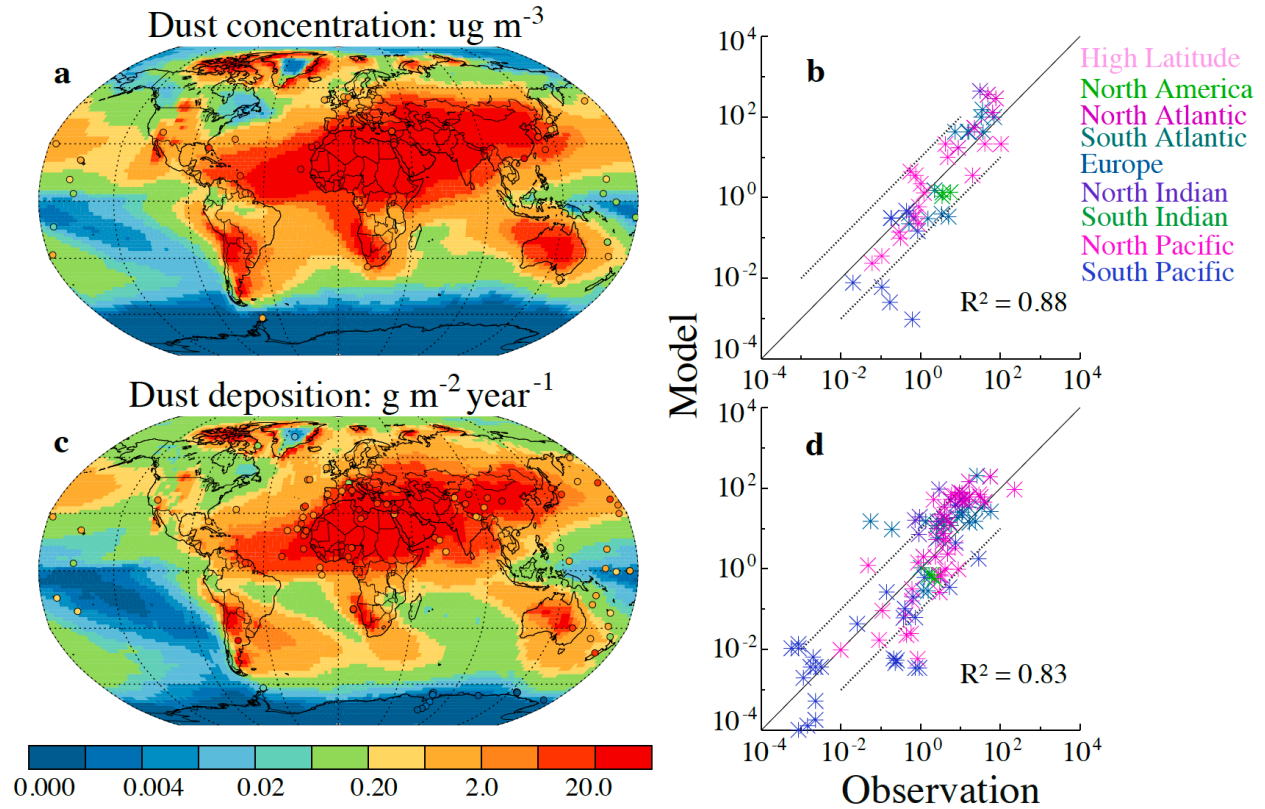


Figure R4. Comparison of simulated (the baseline case; see text for details) dust surface concentration, and deposition with observations. Also shown is correlation (both passed 95% statistically significant tests) between modeling and observations over sub-domains as indicated by texts in color. The dash lines in (b) and (d) represent 10:1 (upper left) and 1:10 (bottom right) lines.

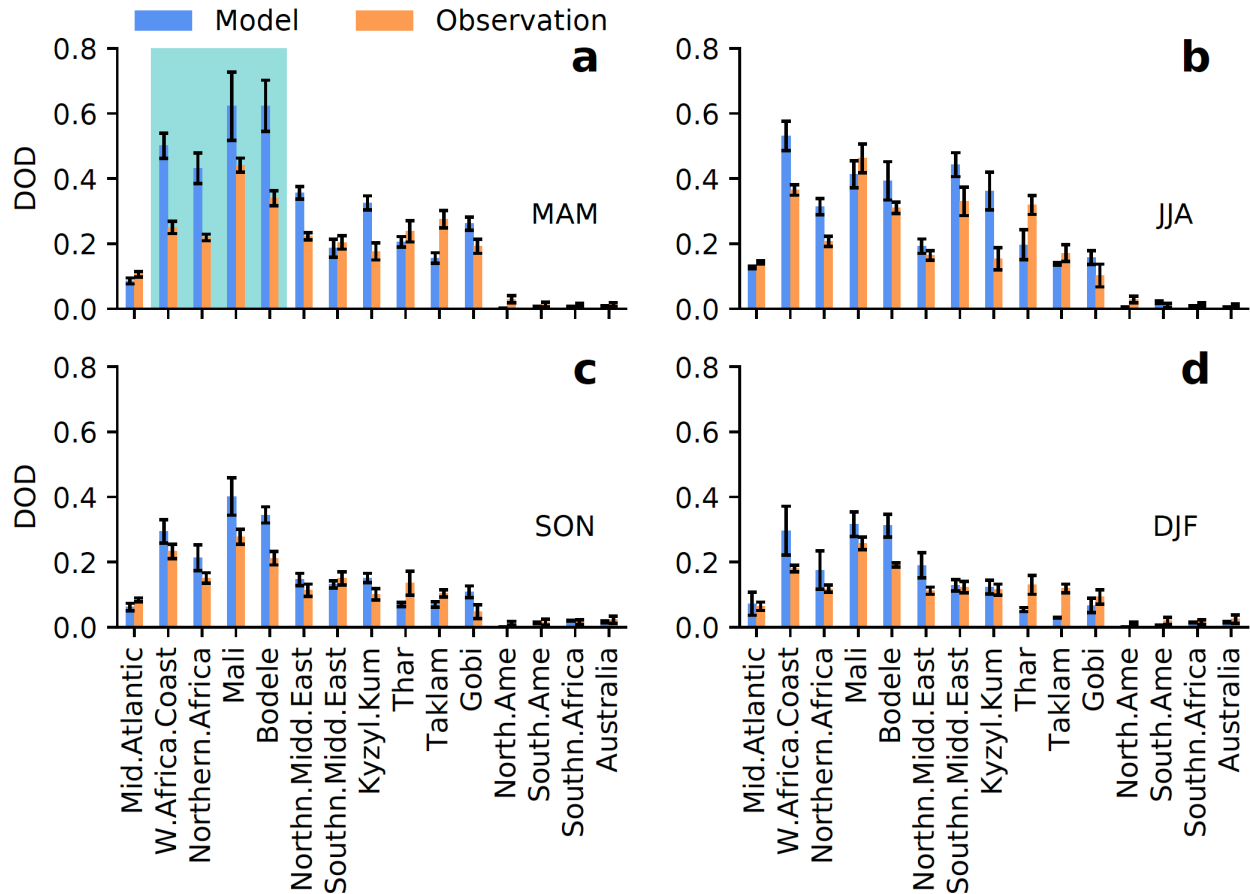


Figure R5. Comparison of seasonally resolved dust aerosol optical depth (DOD) from the baseline simulation (blue) over 15 regions with that (brown) obtained in Ridley et al., (2016) who bias-corrected satellite-based retrievals from the Moderate Resolution Imaging Spectroradiometer (MODIS) and the Multi-angle Imaging Radiometer (MISR) using AEROSOL ROBOTIC NETWORK (AERONET) measurements and a model ensembles (see Ridley et al. 2016 for details). The shading area shows an example that the model greatly overestimated DOD compared to observations. Error bars represent the standard deviation.

Table R2. The climatologically mean total aerosol optical depth (AOD), absorbing aerosol optical depth (AAOD), and single scattering albedo (SSA) at 0.55 μm for AERONET (first portion) and at Band 10 centered at 0.53 μm for CAM5/6 (second portion). Values from CAM5/6 with J2014 (J) and/or C1999 (c) were obtained by averaging modeled AOD, absorbing AOD (AAOD), and SSA over the grid box nearest to the AERONET sites (e.g., Holben et al., 1998) where $\text{DOD} > 0.5 \cdot \text{AOD}$ (DOD represents dust AOD). Values in parenthesis show the standard deviation of AOD, AAOD, and SSA. Other notations: C(J)_bse: the baseline simulation with C1999 (J2014); J_Hig(Low) and J_Low: high(low)-bound of iron oxides in J2014, respectively; C_H(L)HemClay(Silt): high(low)-bound (see text for explanations) hematite in the clay(silt)-sized category; C_H(L)DOD: high(low)-bound DOD; C_H(L)Ima: high(low)-bound imaginary complex refractive index of minerals.

	AOD	AAOD	SSA
AERONET	0.383(0.115)	0.046(0.011)	0.923(0.013)
CAM6	0.209(0.057)	0.035(0.011)	0.899(0.008)
CAM5C_bse	0.205(0.066)	0.039(0.011)	0.891(0.010)
CAM5J_bse	0.205(0.065)	0.046(0.016)	0.875(0.006)
CAM5J_Hig	0.202(0.063)	0.062(0.023)	0.837(0.010)
CAM5J_Low	0.196(0.061)	0.031(0.008)	0.907(0.007)
CAM5C_HHemClay	0.205(0.065)	0.044(0.013)	0.879(0.010)
CAM5C_LHemClay	0.206(0.066)	0.034(0.009)	0.903(0.010)
CAM5C_HHemSilt	0.205(0.065)	0.041(0.012)	0.886(0.010)
CAM5C_LHemSilt	0.206(0.066)	0.048(0.010)	0.896(0.010)
CAM5C_HDOD	0.228(0.075)	0.043(0.012)	0.891(0.010)
CAM5C_LDOD	0.184(0.056)	0.036(0.010)	0.890(0.010)
CAM5C_HIma	0.206(0.066)	0.042(0.012)	0.885(0.010)
CAM5C_LIma	0.205(0.065)	0.037(0.010)	0.897(0.010)